Transient liquid phase bonding of carbon steel components using Ni-based foils - a comprehensive joint characterization

Nicolás Di Luozzo, Michel Boudard, Marcelo Fontana

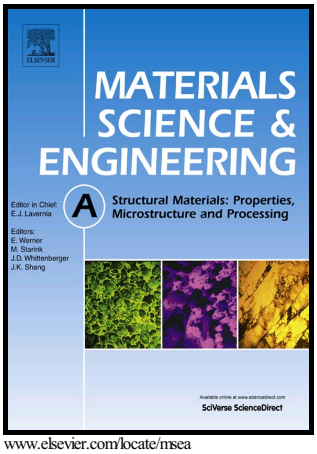

www.elsevier.com/locate/msea

PII: S0921-5093(19)30223-0
DOI: https://doi.org/10.1016/j.msea.2019.02.050
Reference: MSA37569

To appear in: *Materials Science & Engineering A*

Received date: 12 January 2019
Revised date: 15 February 2019
Accepted date: 16 February 2019

Cite this article as: Nicolás Di Luozzo, Michel Boudard and Marcelo Fontana, Transient liquid phase bonding of carbon steel components using Ni-based foils - a comprehensive joint characterization, *Materials Science & Engineering A,* https://doi.org/10.1016/j.msea.2019.02.050

Transient liquid phase bonding of carbon steel components using Ni-based foils - a comprehensive joint characterization

Nicolás Di Luozzo [a,*], Michel Boudard [b], Marcelo Fontana [a]

[a] Laboratorio de Sólidos Amorfos, INTECIN, Facultad de Ingeniería (UBA-CONICET), Paseo Colón 850, C1063ACV Buenos Aires, Argentina

[b] Université Grenoble Alpes, CNRS, Grenoble INP, LMGP, F-38000 Grenoble, France

[*] Corresponding author. ndiluozzo@fi.uba.ar

Abstract

The transient liquid phase bonding (TLPB) process is one of the selected joining technologies to replace threaded connections in solid expandable tubulars. In particular, for expandable hot-rolled seamless carbon steel tubular products using Ni-based amorphous metallic foils as filler material.

In this work, a comprehensive mechanical properties and microstructural characterization was carried out in TLP-bonded bars for this base metal/filler material combination. Both the joint and the heat affected zone exhibited a strength which compares well with the base metal, and a ductility in accordance with that which is typically specified for steel arc-welded joints. A coalesced lath-like bainitic microstructure was found at the joint. In addition, and by means of orientation imaging, a parent austenite grain - which is shared by the joint and an adjacent ferrite grain from the base metal - was found, which demonstrates the epitaxial nature of the TLPB solidification process.

Also, a cell-block-like structure at ferrite grains next to the joint was detected, due to the plastic deformation developed in tensile-tested samples at room temperature.

Keywords

transient liquid phase bonding; carbon steel; amorphous metallic foil; phase transformation; X-ray analysis.

1. Introduction

Solid expandable tubulars (SETs) are being successfully applied in the oil and gas industry [1]. In particular, for reinforcing or repairing existing cased wells, and for cladding uncased portions of wells [2]. In general, SETs comprise strings of hot-rolled seamless steel tubes joined together by threaded connections (TCs) to attain the desired length, whose original inner diameter can be expanded up to 24% [3]. Despite its enormous potential of changing drilling and maintenance operations of current and future wells, the sealing ability of TCs is often significantly diminished as a result of the expansion process. To enhance thread sealing after expansion, ad hoc metal to metal seals [4], protective tubular sleeves [5], and even pre-expanded TCs [6] - to reduce its expansion ration with respect to the body of SETs - have been proposed.

The transient liquid phase bonding (TLPB) process [7] is considered as an alternative joining technique to TCs for SETs. Its main benefit over TCs is its tightness against leakage, with a comparable completion time - which is well below than that of conventional arc welding processes. TLPB involves three main steps: liquefaction of the interlayer and base metal dissolution, liquid phase isothermal solidification, and solute homogenization [8]. Carbon seamless steel SETs were already TLP-bonded using amorphous metallic foils - mostly Ni-based - as interlayers in different conditions (roughness of the contact surfaces, process temperature (hereafter T_P), holding time at T_P (hereafter t_H), protective atmosphere, applied pressure, etc.) [9] [10]. An operating window of the main process parameters was defined to obtain specific requirements at the joint - the zone where both the microstructure and the chemical composition differ from that of the base metal. In particular, for which the tensile strength at the joint outperformed that of the base metal after expansion. However, both microstructure characterization and its relationship with mechanical properties is still incomplete.

TLPB was also applied in other types of steel tubular products. Amorphous foils of the Fe-Ni-Cr-Si-B system were used as interlayers for bonding hot-rolled seamless pipes for boilers [11] and drill pipes [12]. The obtained joints outmatched the tensile strength of the base metals and were successfully bend tested - the latter being fundamental to quantify the ductility of the joint. However, its microstructural characterization was far from being complete, and only limited to show that the presence of undesired phases - which may form during TLPB process as a consequence

of the reaction between the alloying elements of the filler material and the base metal - was negligible.

Regarding microstructure characterization, TLP-bonded seamless carbon steel tubes - both hot-rolled and cold-rolled - were extensively studied for a variety of filler materials: Fe-B [13] and Fe-Si-B [14] [15] amorphous metallic foils, and pure Cu foils [15] [16]. In addition, tensile tests showed that the joined tubes failed away from the joint, attaining almost the ultimate tensile strength (UTS) of the base metal when Fe-Si-B and Cu foils were used.

Concerning the solidification of the transient liquid phase during t_H, epitaxial growth from adjacent grains of the base metal was assumed in all models that describe the TLPB process [7] [8]. However, this phenomenon was rarely observed at the joint [17] [18]. Therefore, the evidences of epitaxial growth are not conclusive, and other solidification processes cannot be discarded (e.g.: constitutional supercooling [19]).

In the present paper, a comprehensive mechanical properties and microstructural characterization of the joint and the adjacent base metal of TLP-bonded hot-rolled carbon steel bars using Ni-based foils as filler materials is presented. The obtained mechanical properties/microstructure relationship is discussed, for one of the selected base metal/filler material combination for TLPB of SETs. In addition, an in-depth crystalline orientation analysis was performed to detect evidences of epitaxial growth during solidification of the transient liquid phase.

2. Materials and Methods

TLP-bonded joints were produced using ASTM A 675 Grade 55 hot-rolled carbon steel bars as base metal, and METGLAS® MBF-30 amorphous Ni-based foils as interlayer (for chemical composition see Table 1). Steel bars had an outside diameter of 25 mm, while the filler material had a thickness of 25 μm.

Table 1. Chemical composition (in wt.%) of the base metal and the interlayer.

	C	Mn	Cr	Mo	B	P	S	Si	Al	Co	Ni	Fe
Grade 55	0.113	0.910	0.028	0.005	0.001	0.016	0.011	0.23	0.007	-	0.018	Bal.

MBF-30	0.009	-	18.81	-	3.006	0.011	0.0018	4.378	0.005	0.03	Bal.	0.389

The bonding process consisted of aligning the bars to be joined - with their abutting surfaces in contact with the interlayer. Before joining, the abutting surfaces were polished using silicon carbide abrasive papers up to #600 grit to attain a roughness average (R_a) of 0.5 µm or below. The assembly was placed into the coil of an induction furnace under a controlled reducing atmosphere (10% H_2 + 90% Ar), while a uniaxial pressure of 5 MPa was applied (Fig. 1). The temperature at the joint was raised to T_P = 1300 ºC, held constant for t_H = 7 min, and then was cooled in still air to room temperature. For further details, see *Di Luozzo et al* [13] [14].

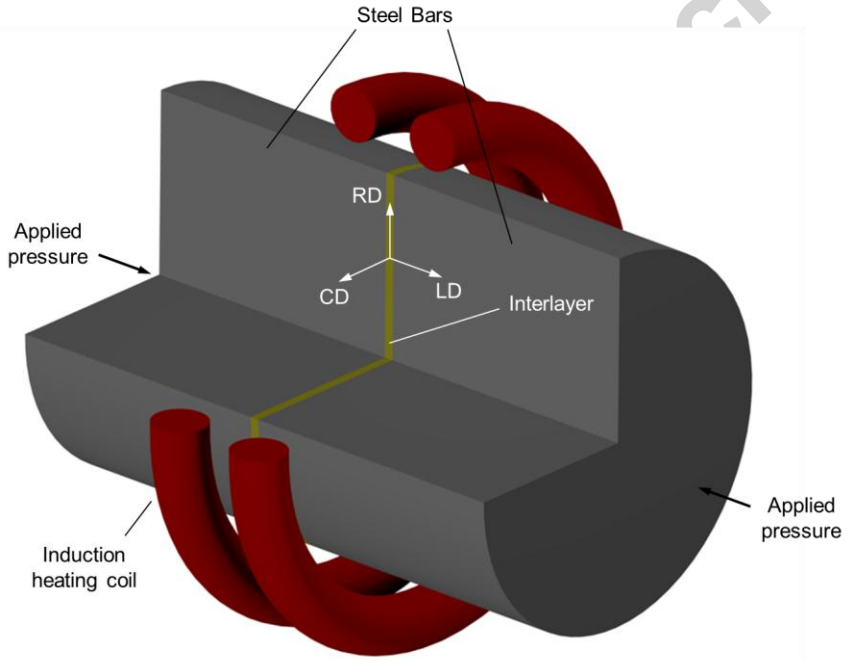

Fig. 1. Schematic illustration of the TLPB process - cutaway perspective view. The abutting surfaces of the bars to be joined are in contact with the interlayer. The longitudinal direction (LD), radial direction (RD) and circumferential direction (CD) are indicated.

Both tensile and bend tests were performed to characterize the mechanical properties of the joint in the as-welded condition in comparison to the base metal. Tensile tests were performed on round specimens in accordance to ASTM E8 [20] (12.5 mm diameter; 50 mm gauge length). Bend tests were carried out on round specimens in accordance to BS EN ISO 7438 (13 mm diameter - *d*; angle of bend: 180º) [21]. The joint was placed at the mid-length of the gauge length and at the mid-point between the supports for tensile and bend test, respectively. In particular, for bend tests, the diameter of the mandrel (*4d:* 52 mm) and the distance between supports (*6d* + 3 mm = 81 mm) were selected to give an outer fibre elongation of 20 % - as it is usually specified for welded joints carried out using conventional arc welding processes [22].

Microstructural characterization was performed by field-emission gun-scanning electron microscopy (FEG-SEM; FEI Quanta 250), transmission electron microscopy (TEM; Philips CM200 with ultra-twin objective lens), and electron backscatter diffraction (EBSD; Zeiss Ultra 55 FEG-SEM equipped with an EBSD detector EDAX DigiView III).

Regarding sample preparation for SEM and EBSD, sections perpendicular to CD were analysed. They were grounded and polished with diamond suspension of 6 and 1 µm. The final polishing varies in each analysis: 0.3 and 0.05 µm alumina suspension followed by etching with 2% Nital solution for FEG-SEM, and 0.05 µm colloidal silica suspension for EBSD. The working voltage of FEG-SEM and EBSD were 15 and 20 kV, respectively.

For EBSD acquisition and analysis, a map step size of 85 nm was used, and data was evaluated using the Oxford Instruments CHANNEL 5 software package. It was performed on already tensile-tested samples to study whether decohesion at the joint/base metal interface had taken place or not. In particular, Euler angles are displayed to depict each point of the obtained orientation imaging (OI) maps. The Bunge convention is used, representing each of the Euler angles (for cubic symmetry: $0º < \varphi_1 < 360º$; $0º < \phi < 90º$; $0º < \varphi_2 < 90º$) with one of the RGB colour channels [1]. Euler angles describe the orientation of the crystal coordinate system with respect to the sample coordinate system. Therefore, Euler colouring of both OI maps and their

[1] Euler space is discontinuous, which can result in small changes in orientation producing abrupt changes in the Euler colouring [52].

associated pole figures enables a direct visual relationship between the position of each point and its orientation [2].

TEM samples were sliced from 3-mm-diameter rods, mechanically thinned to around 200 μm, and then twin-jet electropolished to perforation by a Struers Tenupol-5 twin-jet unit using a 95/5 vol.% solution of acetic and perchloric acids at room temperature at 40 V. Indexing was carried out using Gatan Microscopy Suite® Software.

In addition, quantitative chemical composition analysis was performed by electron probe microanalysis (EPMA; JEOL JXA 8230), with an operating voltage of 20 kV. The uncertainties in the measurements were computed according to the statistical errors in each point analysis, and they were automatically assessed by the acquisition software (JEOL PC-EPMA 1.9.0.3).

Also, in situ X-ray thermodiffraction (XRTD) was performed to determine the austenite transformation temperature range of the present phases at room temperature. XRTD measurement was carried out at the X-Ray scattering and thermomechanical simulation experimental station (XTMS) at the Brazilian National Synchrotron Source (LNLS). The experimental setup consisted of a customized thermal simulator (Gleeble™ 3S50), integrated in a synchrotron X-ray diffraction (XRD) beamline. The monochromatic beam (12 keV, λ = 1.033 Å) was focused down to a full-width half-maximum (FWHM) of 375 μm × 950 μm - in the RD and LD, respectively. The diffraction intensity was measured by two MYTHEN-1K linear detector modules with 1280 channels each. The experiment was performed under vacuum (1×10^{-2} mbar), and the sample was tilted 15º in relation to the incident beam (Fig. 2).

[2] Inverse pole figure colouring depicts the projection of a specific sample direction (e.g.: ND, RD or TD) into the crystal coordinate system at each point of the map. Consequently, its relationship with the pole figure - which represents crystal orientations with respect to a fixed coordinate system - is difficult to understand.

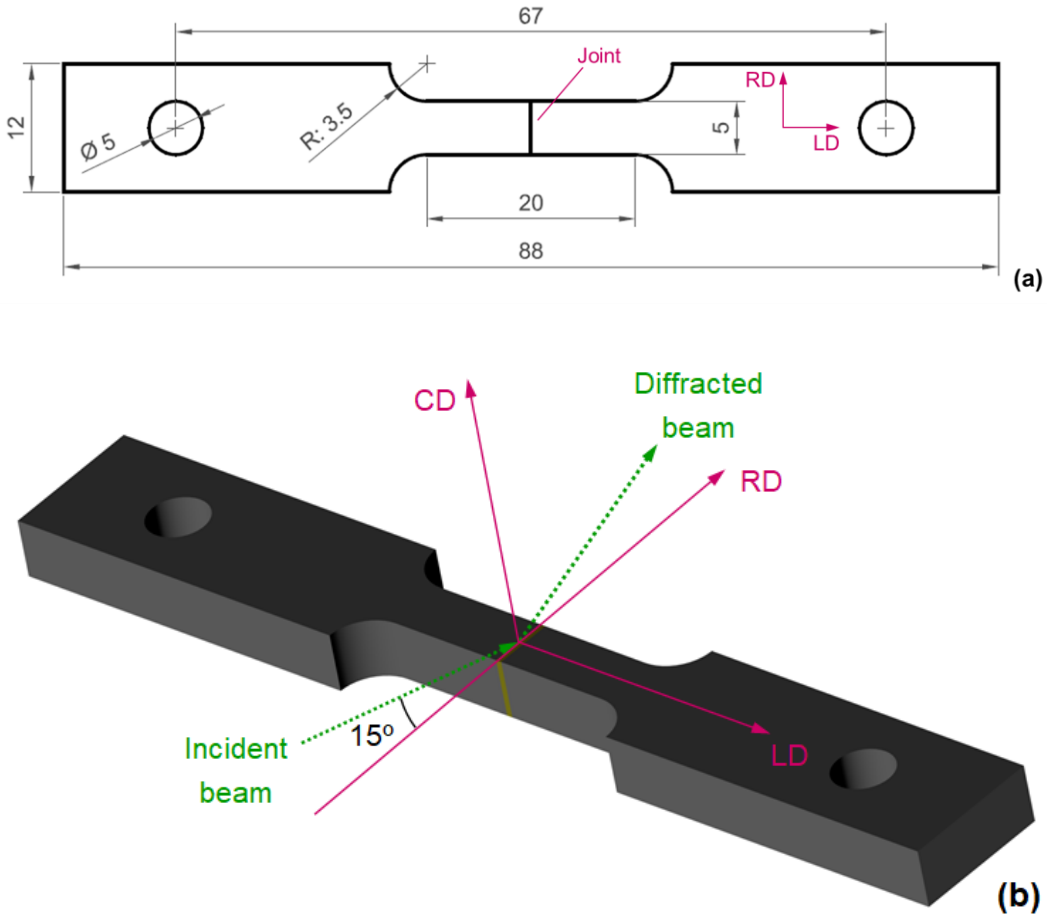

Fig. 2. In situ XRTD measurement. (a) Schematic illustration of the sample used for the experiment - front view, which was cut from the TLP-bonded bar. The dimensions are given in millimetres. (b) Experimental setup. The incident beam - already focused and monochromatized - is aimed at the joint, which is contained in the RD-CD plane of the sample, forming an angle of 15º with respect to RD.

Regarding the thermal cycle, the sample was heated from room temperature to 975ºC. Then, it was cooled down to room temperature by natural convection inside the simulator's chamber. Both the heating and cooling rates were 1ºC/sec. The diffraction data was collected with the sample and linear detectors at a fixed specific position to get XRD patterns every 20 sec in the range of $2\theta = 27^{\circ}$-48°, and was analysed using IgorPro [23] programming suite. Also, before and after the thermal cycle, *initial* and *final* XRD patterns were collected with an acquisition time of 180 sec, with the aim of defining the starting and finishing phases of the analysed region.

3. Results

3.1. Mechanical properties measurement

Table 2 indicates the measured tensile and bend test data, which are the average values of 4 samples from the base metal and TLPB weldments in the as-welded condition. In all tensile-tested weldments, failure occurred well away from the joint, at the heat affected zone (HAZ). Anyway, the average UTS of the weldments attained 98.5 % of that of the base metal. It is noteworthy that it is even possible to improve the obtained UTS by means of a post-weld heat treatment (e.g.: normalizing). While weldments experienced a slight reduction of elongation - due to the coarsened microstructure at the HAZ, both the base metal and the HAZ of the welded samples attained the same reduction of area.

Moreover, samples from the base metal and TLPB weldments were bend tested through 180° without cracking on the outside of the bent portion.

Consequently, TLPB joints exhibited a strength that compares well with the base metal, and a ductility in accordance with what is typically specified for steel arc-welded joints.

Table 2. Tensile and bend test measurements from the base metal and TLPB samples [†].

	UTS (MPa)	Elongation (%)	Reduction of area (%)	Cracking on the outside of the bent portion
Base metal	467 (4)	41.5 (2.0)	72 (0.5)	No cracks observed
TLPB	460 (4)	35.6 (2.0)	72 (0.5)	No cracks observed

[†] Values in brackets indicate standard deviations

3.2. Microstructural analysis

The microstructure at the joint is composed of grains with a lath-like morphology (Fig. 3). Precipitates are observed within most of the laths. However, the size and quantity of precipitates is inhomogeneous. Also, finely spaced pearlite is observed adjacent to the joint.

Considering the thickness of the laths - 1-3 microns, this microstructure can correspond to coalesced bainite [24] and/or coalesced martensite [25]. This type of

microstructure is the result of coalescence of individually nucleated laths with the same crystallographic orientation.

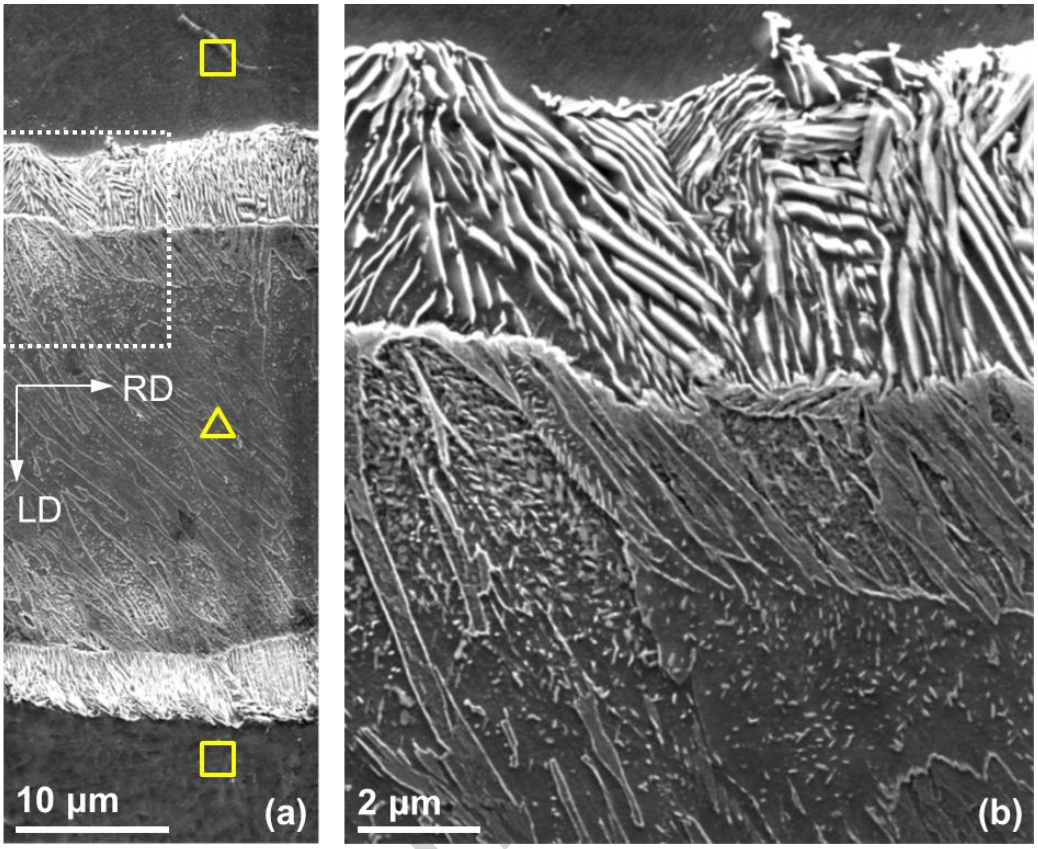

Fig. 3. (a) SEM micrograph of the joint (triangle mark) and the ferrite grains from the base metal adjacent to it (square marks) - in the as-welded condition. Pearlite is visible adjacent to the joint. Also, RD and LD are indicated. (b) Close-up view of the highlighted area (dotted box) in (a). The inhomogeneity in size and quantity of precipitates within laths is shown.

Regarding their precipitates, it is not evident that their longest axes is inclined to a specific direction of the ferrite laths [3]. Also, its length varies in the range from a few tenths to several hundreds of nm (hereafter nano-sized and coarse precipitates, respectively). TEM images combined with its selected-area electron diffraction (SAED)

[3] For the sake of simplicity, laths - that can be composing bainitic and/or martensitic microstructures - are referred as ferrite laths unless otherwise specified.

analysis confirm that precipitates are cementite (Fig. 4). The Isaichev orientation relationship (OR) [26] was confirmed between cementite and ferrite laths:

$$\left(\bar{1}03\right)_{Fe_3C} \,//\, (110)_{\alpha} \qquad [311]_{Fe_3C}\ 0.91^{o}\ \text{from}\left[1\,\bar{1}1\right]_{\alpha}$$

Since in the proposed microstructures for the joint precipitates are cementite, none of them can be discarded.

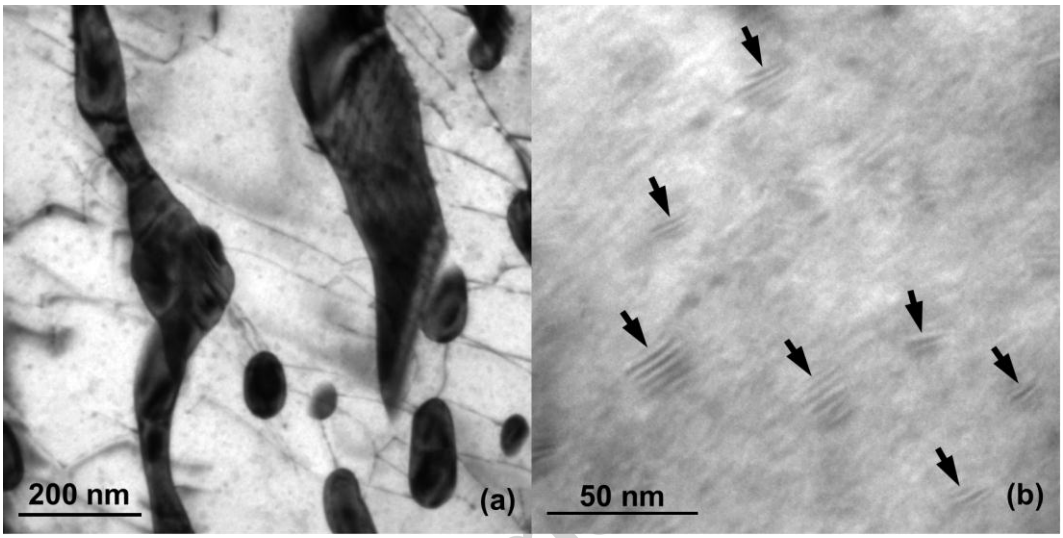

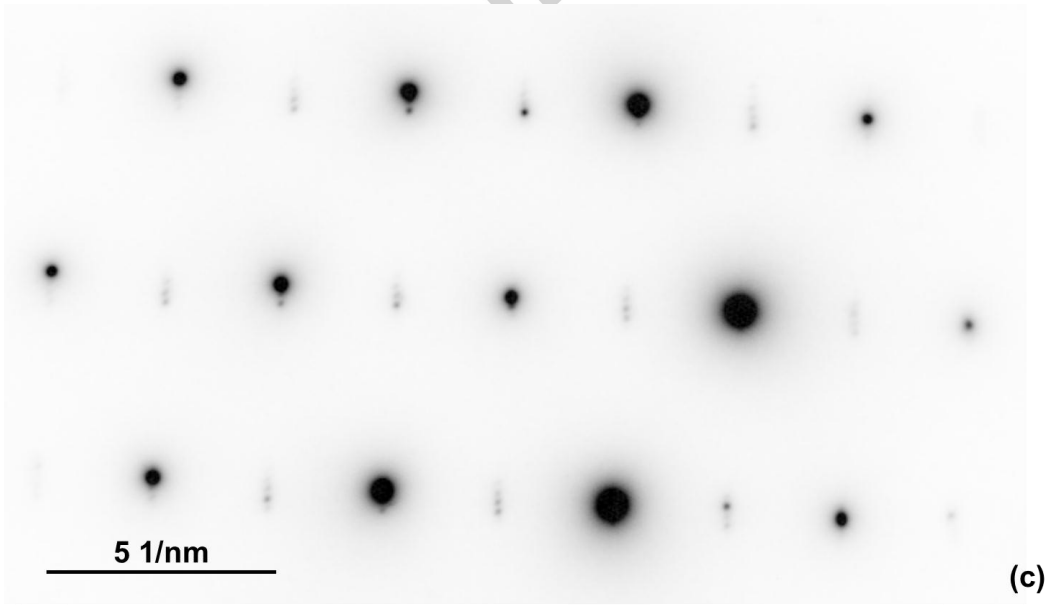

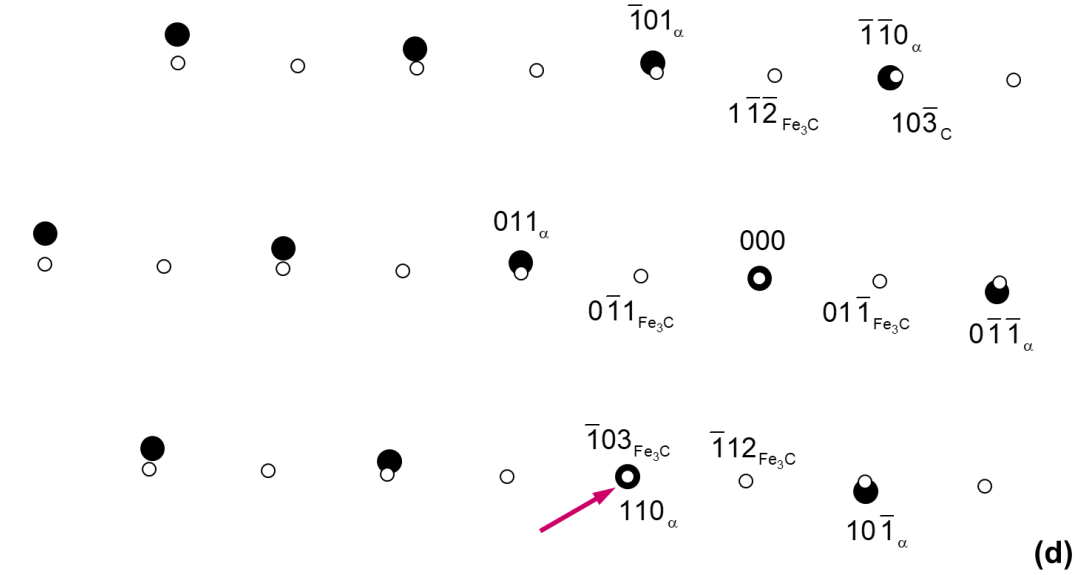

Fig. 4. TEM micrographs of the joint. (a) Coarse precipitates (dark contrast) in a ferritic matrix (bright contrast). (b) Nano-sized precipitates (arrow marks) within a ferrite lath. (c) SAED pattern corresponding to (b) (zone axis: $[311]_{Fe_3C} \approx [1\bar{1}1]_{\alpha}$). (d) Indexing of the diffraction pattern (open circles: precipitate reflections; solid circles: ferrite reflections). The arrow mark indicates $(\bar{1}03)_{Fe_3C}$ // $(110)_{\alpha}$.

3.3. Chemical analysis

EPMA chemical composition measurements show a joint enriched with Ni, Cr and Si from the filler material (Fig. 5). The composition profiles resemble those at some stage of TLPB solute homogenization process [14], very similar to that of planar solid-state diffusion for a source of limited extent. Likewise, the joint is impoverished in Mn.

At the joint, the least amount of alloying elements from the filler material are at its interface with the base metal: 1.8Ni, 1.2Cr, 0.8Mn, 0.4Si (wt.%) (Fig. 5, dashed lines).

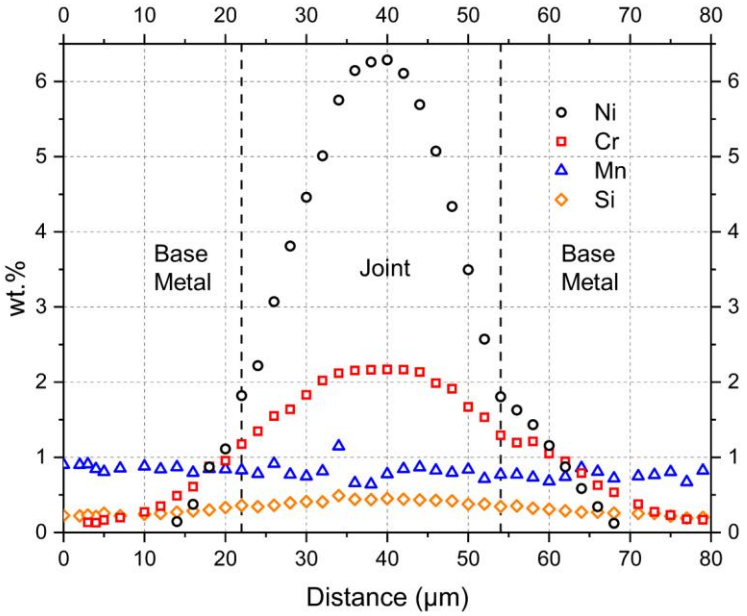

Fig. 5. EPMA chemical composition profiles across the joint and the adjacent base metal. Dashed lines indicate the interfaces between the joint and the base metal (error bars are not shown since they are smaller than the data markers).

It is worth noting how Cr diffused deeper into the base metal compared with Ni, for the same thermal cycle. This is directly connected with their diffusion in austenite at 1300 ºC - $D_{Cr} \approx 2 \times 10^{-13}$ m^2/sec [27] and $D_{Ni} \approx 2 \times 10^{-14}$ m^2/sec [28], supporting the assumption that isothermal solidification and solute homogenization are controlled by solid-state diffusion [8].

3.4. In situ XRTD

Fig. 6 shows the obtained *initial* and *final* XRD patterns. Regarding the detected phases, ferrite is present in both scans. Also, magnetite (Fe_3O_4) reflections are detected (Fig. 6 (b)). This is the result of the thin oxide scale that built up over the sample's surface during XRD thermal cycle.

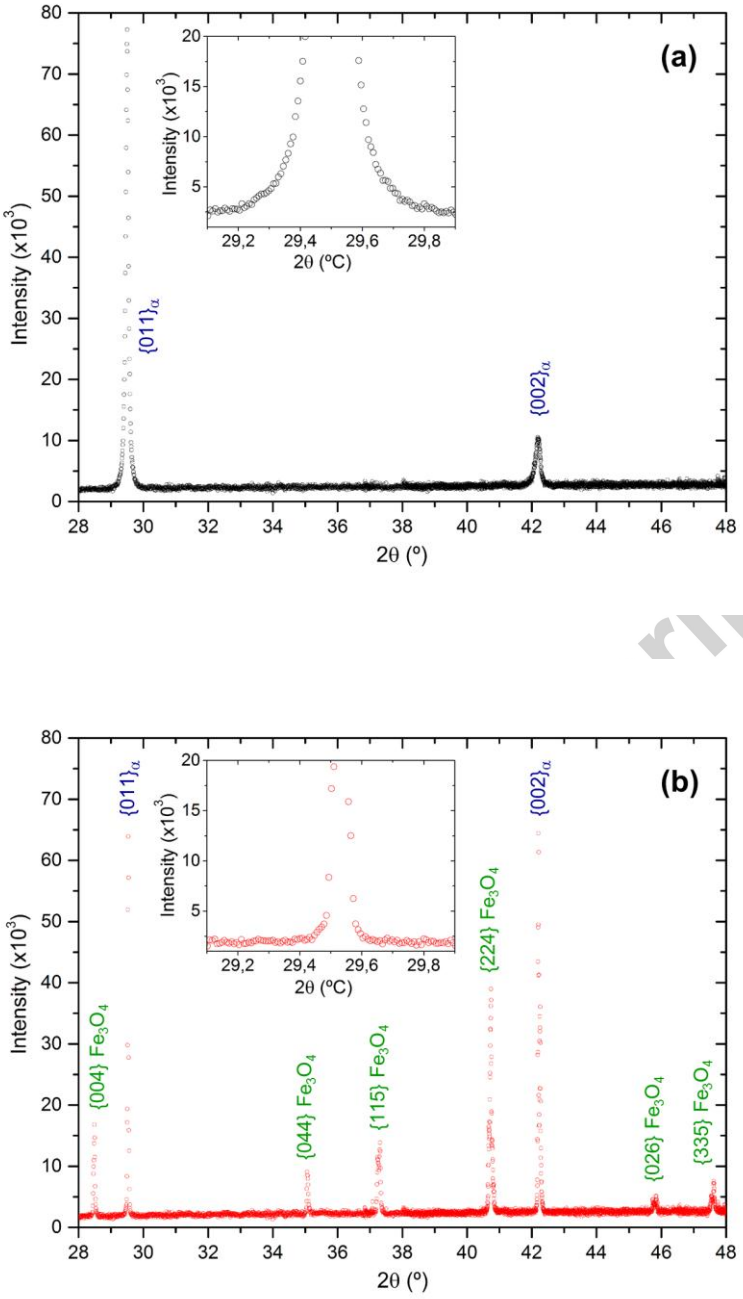

Fig. 6. *Initial* (a) and *final* (b) XRD at the joint and its adjacent base metal, where in situ XRTD was carried out. Inserts: magnification of $\{011\}_\alpha$ peak.

Ferrite reflections can come from all the observed microstructures: ferrite grains and pearlite form the base metal, and ferrite laths from the joint. In order to be able to differentiate them, phase transformations from the austenite phase during cooling from

975 ºC were studied within 2θ = 29-34º. In this angular range, $\{011\}_\alpha$ and $\{002\}_\gamma$ peaks can be clearly identified.

During cooling, four stages can be identified (Fig. 7):

- Between 975 ºC and the start temperature of ferrite formation of the base metal (Ar_3) - 855 ºC [29]: only $\{002\}_\gamma$ is observed, with a splitting behaviour. This phenomenon was reported in carbon [30] and low-alloy steels [23], and Fe-Ni-C alloys [31], indicating the presence of two austenite populations (hereafter γ_1 and γ_2).
- Between Ar_3 and the finish temperature of ferrite formation of the base metal (Ar_1) - 650 ºC [29]: along with the appearance of $\{011\}_\alpha$ peak, two austenite populations are still observed. One is separated from those observed in the previous stage - γ ', vanishing at Ar_1. The other one can be identified as γ_2.
- Between Ar_1 and 405 ºC: together with $\{011\}_\alpha$, only γ_2 persists, which it is detected down to a temperature of 405 ºC.
- Below 405 ºC: only $\{011\}_\alpha$ peak is observed.

Concerning the inherent instrumental resolution - that is to say, the limiting angular separation of diffracted peaks to be separately resolved - is calculated in a similar manner as *Stone et al* [32]. For a given reference phase, FWHM of its peaks are determined. And the resolution is taken as one-third of the FWHM of the peak at the lowest angle at which diffraction data is acquired. To that end, $\{011\}_\alpha$ reflection obtained during the cooling stage was selected as the reference peak and phase. Its refinement - compared with the starting ferrite - is evident in Fig. 6. The FWHM of $\{011\}_\alpha$ from *final* XRD is 0.033º. This corresponds to an angular resolution of 0.011º, and a resolution in the austenite lattice parameter of 0.0013 Å.

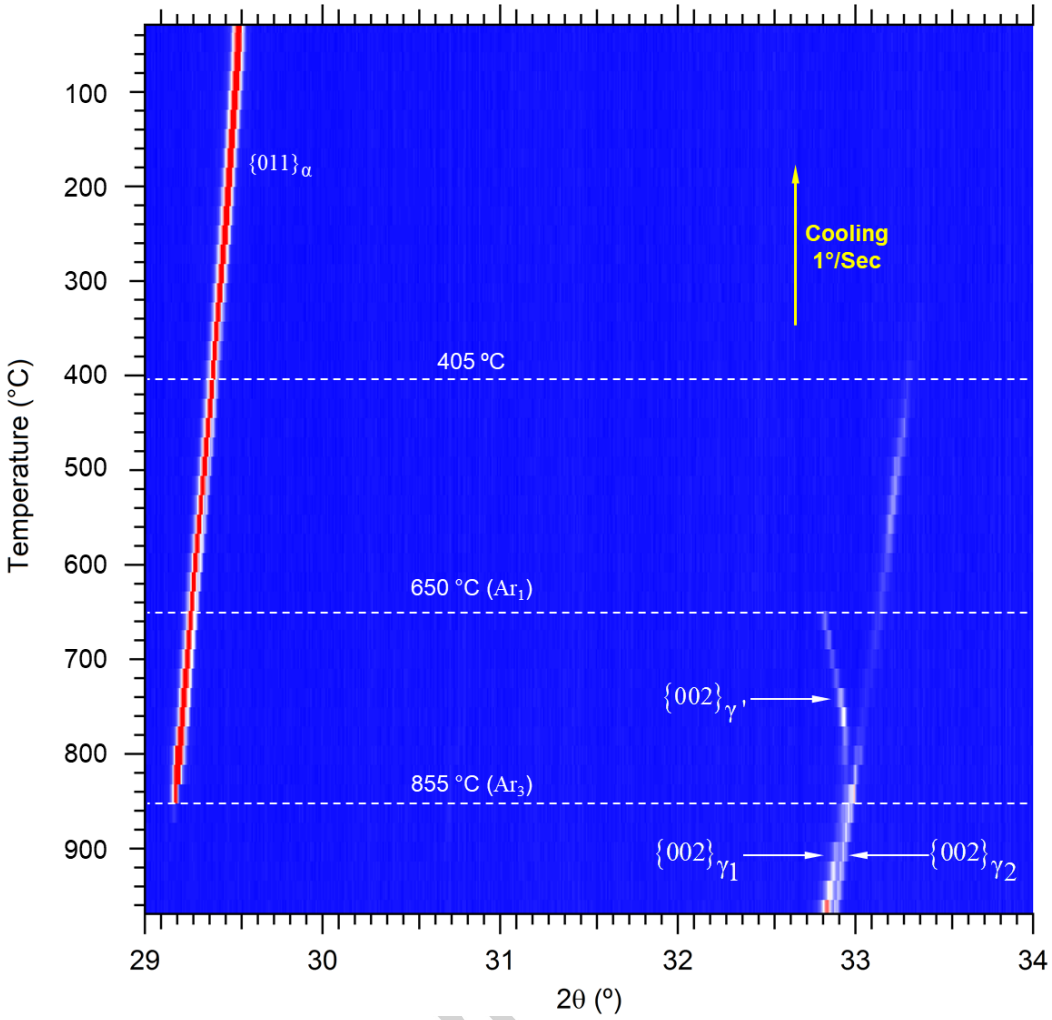

Fig. 7. In situ XRTD at the joint and the adjacent base metal. 2θ vs. temperature (angular range: 29º to 34º; temperature range: 975 ºC to room temperature). The red colour corresponds to higher intensities and blue to lower intensities (background). The critical temperatures of the base metal on cooling (Ar_3 & Ar_1) and the temperature to which $\{002\}_\gamma$ is detected are also indicated.

3.5. Orientation analysis

Euler-coloured OI maps and their associated pole figures are shown in Fig. 8 and Fig. 9, which were carried out at different positions of the joint and the adjacent base metal. Considering the observed microstructures by SEM, ferrite was selected to perform phase identification.

Fig. 8 (a) and (b) show the OI map and its associated $\{100\}_\alpha$ pole figure obtained from the joint, together with the adjacent base metal. This OI map was taken over a large area (70 x 45 μm^2) from a sample in the as-welded condition and after being tensile tested. Since all samples failed away from the joint under tensile tests, it allows the microstructural analyses of the joint after being stressed to the UTS.

Ferrite laths with close crystallographic orientations are distinguished at the joint by means of Euler colouring. However, the orientation of each lath is fairly scattered. Consequently, ferrite blocks - aggregations of laths with close crystallographic orientations - are not always evident, and its boundaries were even more difficult to determine.

Fig. 8 (c) shows the $\{100\}_\alpha$ pole figure corresponding to the joint region of Fig. 8 (a), together with the predicted Kurdjumov-Sachs (KS) orientation relationship (OR) [33]:

$$\{111\}_\gamma \,//\, \{011\}_\alpha \qquad \langle 110\rangle_\gamma \,//\, \langle 111\rangle_\alpha$$

leading to 24 crystallographic variants, and Nishiyama-Wassermann (NW) OR [34]:

$$\{111\}_\gamma \,//\, \{011\}_\alpha \qquad \langle 112\rangle_\gamma \,//\, \langle 110\rangle_\alpha$$

which implies 12 crystallographic variants, from a single crystal (grain) of austenite [4]. Both KS and NW ORs between lath bainite/martensite and austenite are known in steels, and its crystallographic variants are numbered according to *Kitahara et al* [33]-[34]. Ferrite laths orientations are distributed continuously close to both KS and NW variants - usually < 5º, and up to about 10º. It is worth noting that as the austenite is not present at room temperature, it is impossible to directly measure the OR between ferrite laths and austenite. However, since KS and NW OR are fixed, the misorientation between predicted variants can be determined uniquely [35] [5]. Thus, ferrite laths from the joint of the scanned area were formed from a single parent austenite grain.

[4] Crystallographic variant prediction was carried out using PTCLab software [53].

[5] The misorientation is defined as the difference in orientation between two neighbouring points from different crystals.

The $\{100\}_{\alpha}$ poles of one of the coarse neighbouring ferrite grain (Fig. 8 (a), square mark) are illustrated in Fig. 8 (d), together with the already predicted KS and NW variants for the joint. Despite its strong orientation spread due to plastic deformation produced during tensile test, the mean grain orientation is close to KS variants 21 and 24 and NW variant 12 of the joint. Since near KS OR were also reported for proeutectoid ferrite grains [36], both the joint and this coarse ferrite grain belonged to the same parent austenite grain. This highlights the epitaxial nature of the TLPB process.

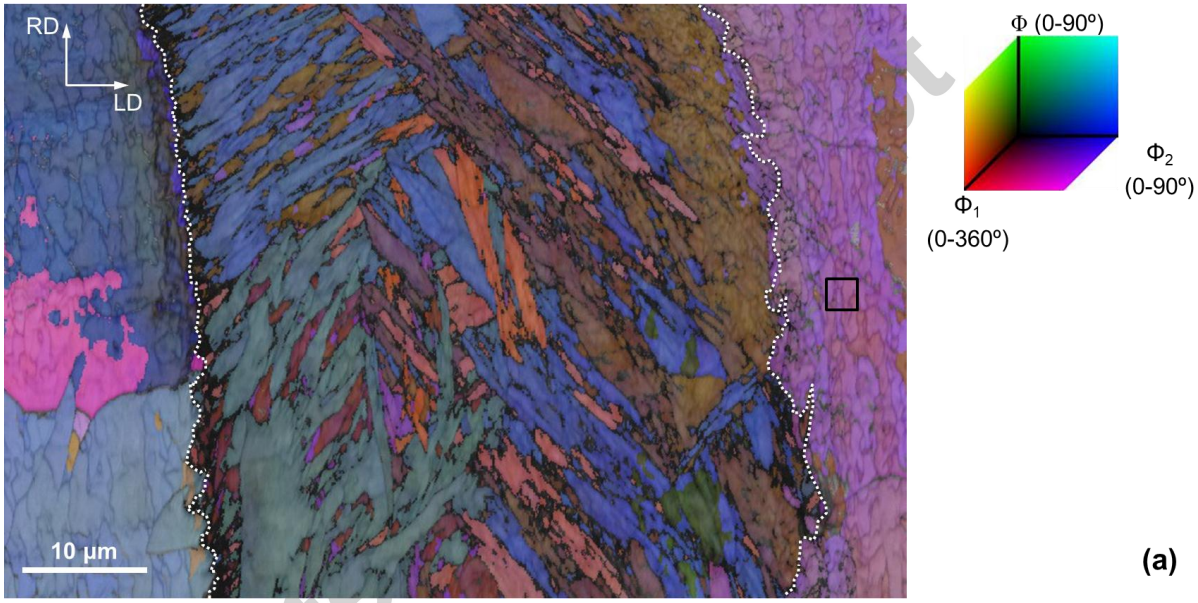

(a)

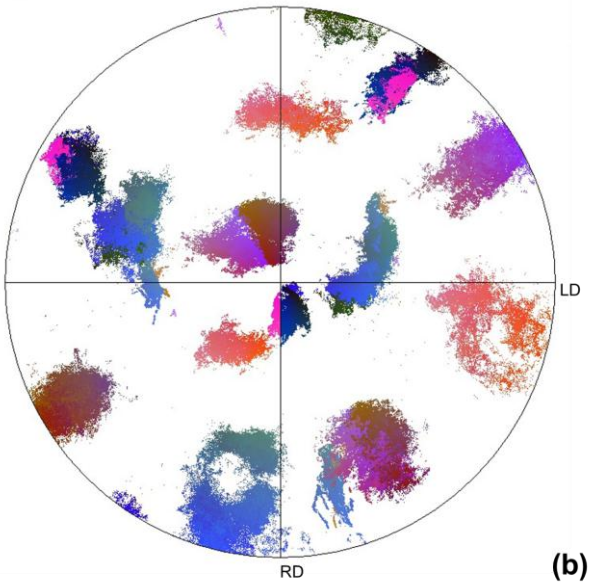

(b)

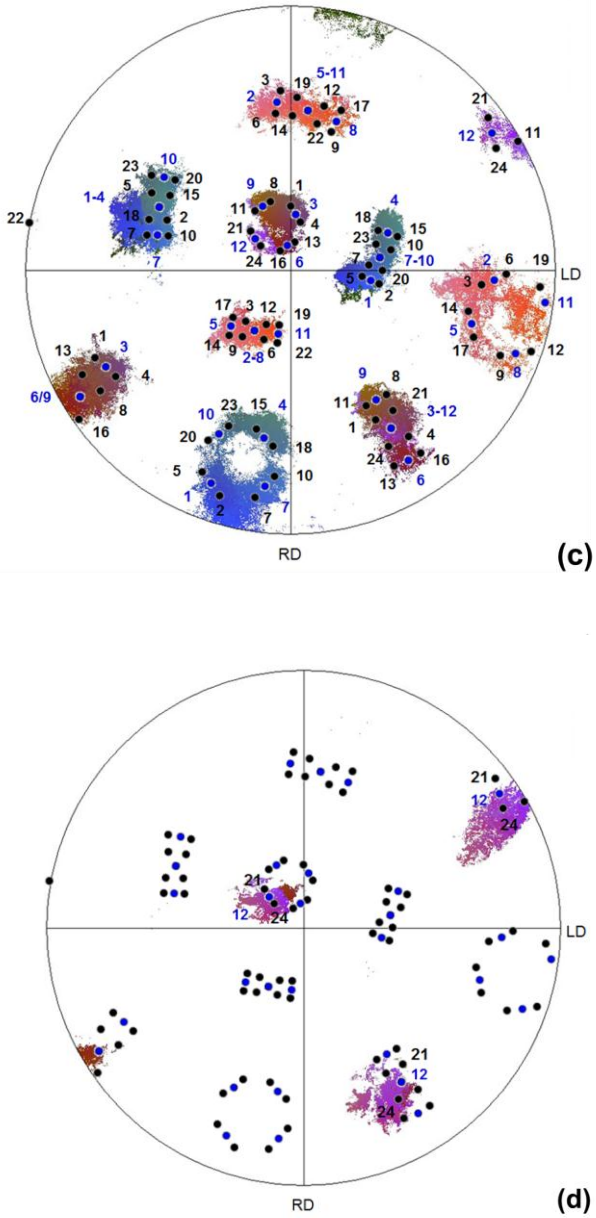

Fig. 8. (a) Euler-coloured OI map - together with the colour space used for the Euler angle description, overlaid on the band slope map (BS) [6]. The white dotted lines approximately delineate the joint region, while a square mark indicates one of the neighbouring coarse ferrite grains. Also, RD and LD are indicated. (b) Euler-coloured $\{100\}_{\alpha}$ pole figure. (c) Euler-coloured $\{100\}_{\alpha}$ pole figure of ferrite laths at joint, together with the predicted KS and NW variants (black and blue dots, respectively). (d) Euler-coloured $\{100\}_{\alpha}$ pole figure of the coarse neighbouring ferrite grain indicated in

[6] BS is an image quality factor which describes the maximum intensity gradient at the margins of the Kikuchi bands in an EBSD pattern [54].

(a), together with the predicted KS variants 21 and 24 (black dots) and NW variant 12 (blue dots).

On the other hand, the coarse ferrite grains of the base metal adjacent to the joint seem to be aggregations of numerous subgrains (Fig. 8 (a), square mark). This is also illustrated in Fig. 9, which shows another position of the joint and its adjacent coarse ferrite grain. This grain is composed of several subgrains, delineated mostly by low angle grain boundaries (LAGB) (Fig. 9 (a)). Moreover, $\{100\}_{\alpha}$ pole figure shows a strong and at the same time continuous orientation spread of this grain (Fig. 9 (b)).

In addition, and despite the abrupt change in microstructure, decohesion of the joint/base metal interface is not observed, despite having been tensile-tested.

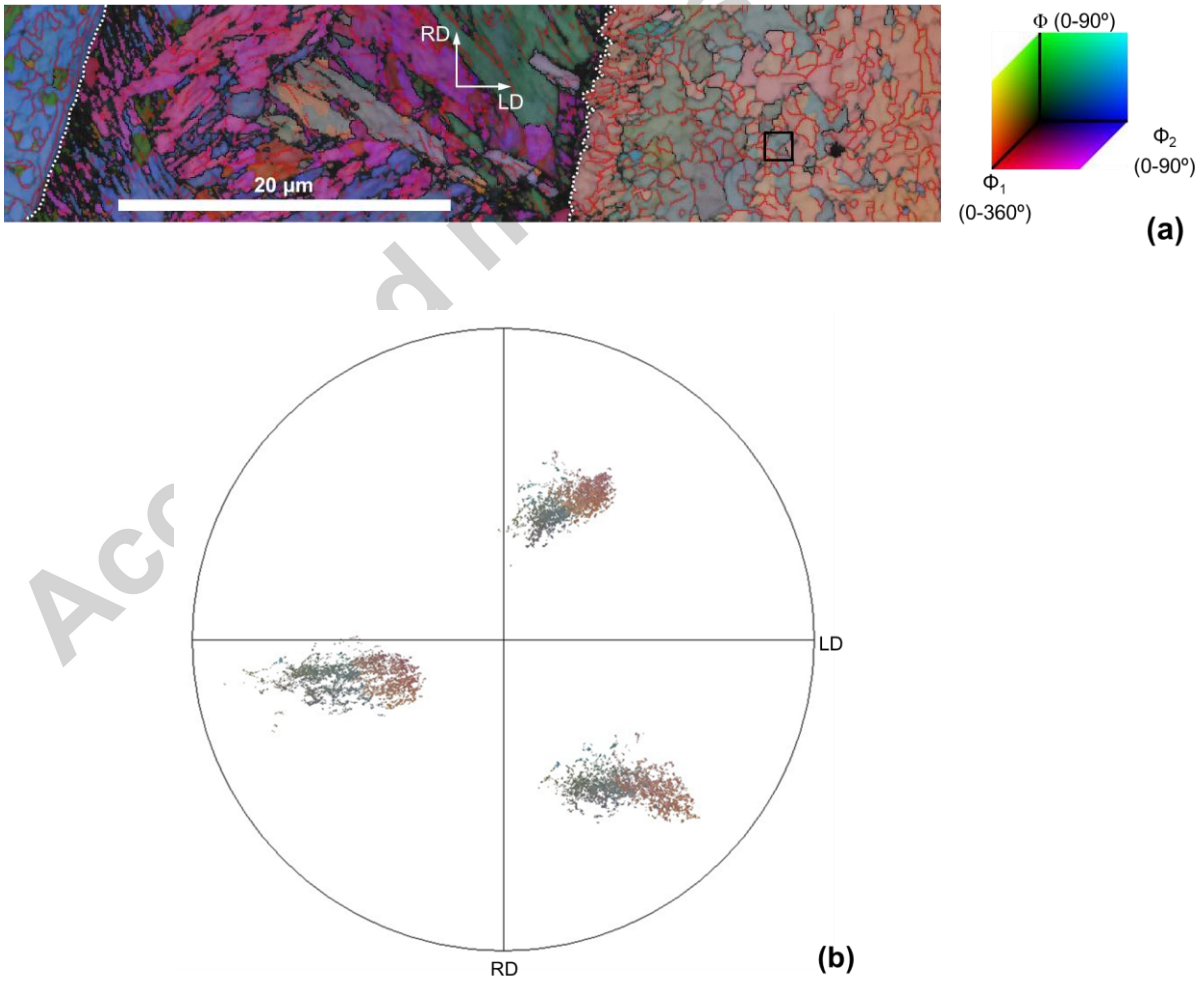

Fig. 9. (a) Euler-coloured OI map - together with the colour space used for the Euler angle description, overlaid on the BS map. The white dotted lines approximately delineate the joint region, while a square mark indicates one of the neighbouring coarse ferrite grains. The red and black lines denote LAGB ($3 < \theta < 15$, where θ is the misorientation angle) and high angle grain boundaries ($\theta > 15$), respectively. Also, RD and LD are indicated. (b) Euler-coloured $\{100\}_\alpha$ pole figure of the neighbouring coarse ferrite grain indicated in (a).

4. Discussion

4.1. Joint and base metal contribution to in situ XRTD

As it is mentioned in section 3.4, different austenite populations are observed in the temperature range from Ar_1 to 405 ºC. It is of great importance to identify the position of each austenite population at the weldment - the joint and/or the base metal. To that end, we will determine the relationship between lattice parameter and thermal expansion of austenite with temperature and chemical composition.

If we restrict to the effects of C and Mn, the equation which provides the best fit to measured data for the compositional dependence of the austenite lattice parameter at room temperature a_γ^r is given by [37]:

$$a_\gamma^r = 3.5667 + 0.033X_C + 0.00095X_{Mn} \qquad (1)$$

where a_γ^r is in Å, and X_C and X_{Mn} are in wt.%. The influence of other alloying elements (e.g.: Ni , Cr, Si, etc.) on a_γ^r can be neglected [38] [7].

Regarding the thermal expansion of austenite, the relative length change $\Delta L_\gamma / L_\gamma^0$ is calculated with the equation given by *van Bohemen* [39]:

[7] The reported maximum solubility of B in austenite vary between 80 and 260 ppm. Since the presence of borides is not observed, it is assumed that B content from the filler material are below the above-mentioned range. Thus, the influence of B on the lattice parameter of austenite in the range of tens of ppm is assumed to be negligible.

$$\frac{\Delta L_\gamma}{L_\gamma^{\,0}} = \frac{L_\gamma - L_\gamma^{\,0}}{L_\gamma^{\,0}} = \beta_\gamma T + \beta_\gamma \Theta_\gamma^{\,D}\left[\exp\left(-\frac{T}{\Theta_\gamma^{\,D}}\right) - 1\right] \quad (2)$$

where $L_\gamma^{\,0}$ is defined as the length of a sample with an austenite lattice at 0 K, T is the absolute temperature (in K), β_γ = 24.8 x 10^{-6} K^{-1}, and $\Theta_\gamma^{\,D}$ is the Debye temperature of austenite (280 K). Since $\Delta L_\gamma / L_\gamma^{\,0}$ proved to be similar to that of Fe for small additions of alloying elements, it is considered compositional independent and the austenite lattice parameter a_γ can be calculated by:

$$a_\gamma = a_\gamma^{\,r}\left(1 + \frac{\Delta L_\gamma}{L_\gamma^{\,0}}\right) \quad (3)$$

Gradients in Mn concentration at the joint and the adjacent base metal were measured by EPMA (Fig. 5). Considering the maximum and minimum content of Mn at the base metal and the joint (0.92 and 0.64 wt.%, respectively), we obtain from Eq. (1) that it represents a change in $a_\gamma^{\,r}$ of 0.0003 Å. This change in $a_\gamma^{\,r}$ is well below the experiment resolution. Therefore, a_γ is given by Eq. (3) assuming that X_{Mn} equals that of the base metal.

Regarding C content gradients, its diffusion distance δ_C is calculated between the finish temperature of austenite formation on heating (Ac_3) and Ar_3 [8], which is given by [40]:

$$\delta_C = \left[\int D_C(T)\frac{dT}{dT/dt}\right]^{1/2} \quad (4)$$

where D_C is the C diffusion coefficient in austenite in m^2/sec, and dT/dt is the rate of temperature change in ºC/sec.

Considering the constant rate of heating to 975ºC and cooling to room temperature (1ºC/sec), D_C can be expressed as [41]:

[8] At the base metal, only austenite exists in this temperature range. Moreover, the joint is enriched in Ni and Cr, which are austenite stabilizers. Thus, the joint is also austenized between Ac_3 and Ar_3.

$$D_c = 1.32\times10^{-3}\left(1+y_C(1-y_C)\left(\frac{5070}{T}+2.7795\right)\right.$$
$$\left.\times\exp\left(-\left(\frac{1}{T}-2.221\times10^{-4}\right)(15182-26083\,y_C)\right)\right. \qquad (5)$$
$$y_C = x_C/(1-x_C)$$

where x_C is the atomic fraction of C in austenite. From equations (4) and (5), and for a C content equal to that of the base metal (0.113 wt.%), we obtain δ_C = 45.5 µm. Thus, δ_C compares well with the joint's width, and a uniform C distribution can be assumed at the joint.

In Fig. 10, the measured a_γ are plotted against temperature for each austenite population observed in Fig. 7 - from 975 ºC to 405 ºC, from which we can highlight:

- Above Ar_3, γ_1 and γ_2 come from C-enriched and C-unenriched austenite populations - of 0.21 wt.% C and 0.09 wt.% C provided by Eq. (3), respectively. It is noteworthy that the mean C concentration of the base metal is almost coincident - within the instrument resolution - with that of γ_2. Regarding the contribution of the base metal to γ_1 and γ_2, this is the result of an incomplete austenization process, which led to a nonhomogeneous distribution of C in the austenite phase. The C-enriched and C-unenriched austenite populations were formed from pearlite and proeutectoid ferrite [30].
- At Ar_3, γ ' shows an abrupt change in slope of austenite lattice parameter with temperature compared with γ_1 and γ_2. This phenomenon is due to C enrichment of austenite during austenite-to-ferrite transformation of the base metal [42]. At Ar_1, a_γ reaches 3.655 Å, corresponding to X_C = 0.96 wt.%. Despite this value is above the eutectoid composition of the metastable Fe-C phase diagram - 0.77 wt.% C [43], concentrations above 1 wt.% C in retained austenite are reported elsewhere [37]. However, γ_2 is still observed. Consequently, this austenite population has an additional contribution: the joint.
- γ_2 starts increasing its C content at 560 ºC, and finally vanishes at 405 ºC. Therefore, a C diffusion-controlled austenite transformation at the joint takes place in this temperature range.

By means of microstructural characterization, it was not possible to discern between coalesced bainite and coalesced martensite at the joint. However, this can be

determined analysing the start temperature of bainite and martensite formation (B_s and M_s, respectively). B_s and M_s can be calculated as follows [44],[45]:

$$B_S = 745 - 110X_C - 59X_{Mn} - 39X_{Ni} - 68X_{Cr} - 106X_{Mo} + 17X_{Mn}X_{Ni} + 6X_{Cr}^2 + 29X_{Mo}^2 \quad (6)$$

$$M_S = 491.2 - 302.6X_C - 30.6X_{Mn} - 14.5X_{Si} - 16.0X_{Ni} - 8.9X_{Cr} + 2.4X_{Mo} + 8.6X_{Co} \quad (7)$$

where B_S and M_S are in ºC, and X_i are in wt.%.

Considering the chemical composition gradient at the joint, we proceed as follows. Except the slight reduction in Mn, the joint is enriched in austenite stabilizers - mainly Ni and Cr, which lower the start temperature of austenite transformation. In particular, the least amount of austenite stabilizers takes place at the interface between the joint and the base metal - with a mean chemical composition of 0.09C, 1.8Ni, 1.2Cr, 0.8Mn, 0.4Si (wt.%), as it was pointed out in section 3.3. Therefore, at this position both B_S and M_S are maximum. From Eq. (6) and (7) we obtain B_S = 566 ºC and M_S = 387 ºC, respectively. B_S is almost coincident with the observed start temperature of a C diffusion-controlled austenite phase transformation, and well above M_S. Consequently, austenite-to-bainite transformation takes place at the joint - in particular, into coalesced bainite.

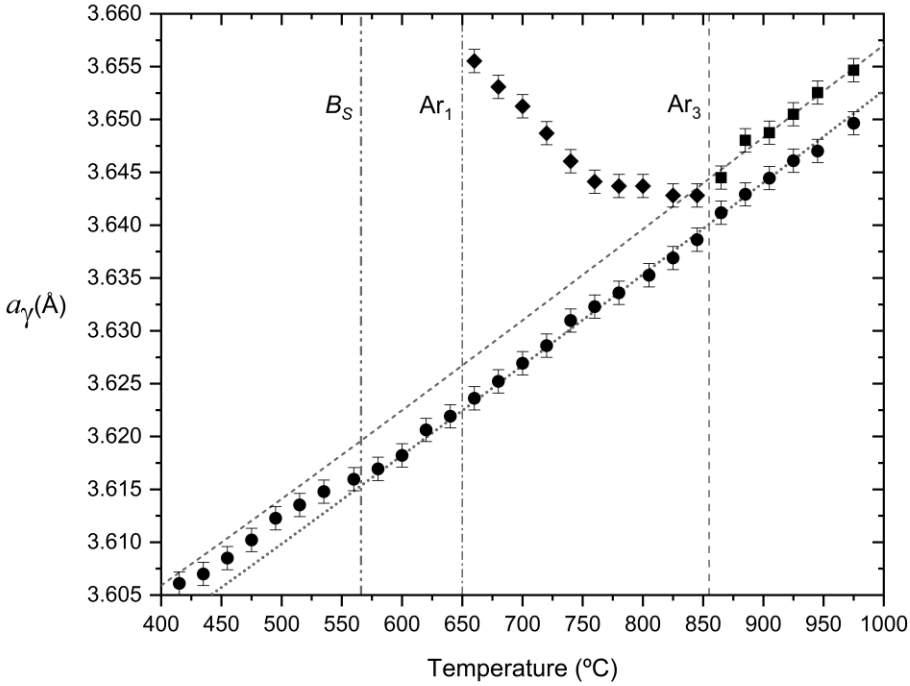

Fig. 10. a_γ vs. temperature during cooling. γ_1 (square marks) and γ_2 (circle marks) are shown from 975ºC to Ar_3. Below Ar_3, γ' (diamond marks) and γ_2 are also shown. The dotted and short-dashed lines represent a_γ provided by Eq. (3) for 0.09 and 0.21 wt.% C, respectively. Both Ar_1 and Ar_3 from the base metal are indicated, in addition to the calculated B_S at the joint/base metal interface. Error bars show the calculated instrument resolution - 0.0013 Å.

4.2. Orientation imaging analysis

4.2.1. Orientation relationship between bainite laths at the joint

From Fig. 8 (c), it is evident the orientation spread within each ferrite lath at the joint, which includes two coplanar KS variants (that is, with the same $\{111\}_\gamma$ parent austenite plane) with the minimum misorientation - 10.53º around $\langle 110 \rangle_\alpha$ axis, together with the intermediate NW variant (e.g.: KS variants V1-V4 with NW variant V3, respectively). In addition, variant selection is not evident since the measured orientations are spread over almost all the predicted KS and NW variants. Moreover, the deviation of ferrite laths from KS and NW ORs is mostly distributed between 0º and 5º -

and up to 10º. Thus, OI characterization is very similar to that reported from proeutectoid ferrite [36], lath martensite [35] and bainite [46] in steels, to Fe-Ni alloys [34], although in our work the sample had already been tensile tested.

On the other hand, variant selection between ferrite laths is detected by means of the misorientation distribution function (MDF) [9]. The misorientations with the highest frequency were found for angles in the range of 58-60º (Fig. 11): a primary peak at $\langle 111 \rangle$/60º, together with a much less secondary peak at $\langle 101 \rangle$/60º. Considering that $\langle 111 \rangle$ /60º misorientation is only predicted by KS OR [33], it is evident that it better describes the measured OR. *Morito et al* [35] reported $\langle 101 \rangle$/60º as the misorientation with the highest frequency for block boundaries for lath martensite in a broad range of C concentration. However, in this work MDF includes misorientations between laths, blocks and packets - aggregations of blocks with the same $\{111\}_\gamma$ plane in the parent austenite grain.

Consequently, a near KS OR - with $\langle 111 \rangle$/60º as the misorientation with the highest frequency - is more representative than that both the KS and NW ORs are obeyed without any variant selection.

[9] MDF depicts the frequency of misorientation axis/angle pairs within the fundamental zone - i.e.: using the minimum angle/axis pair representation [55].

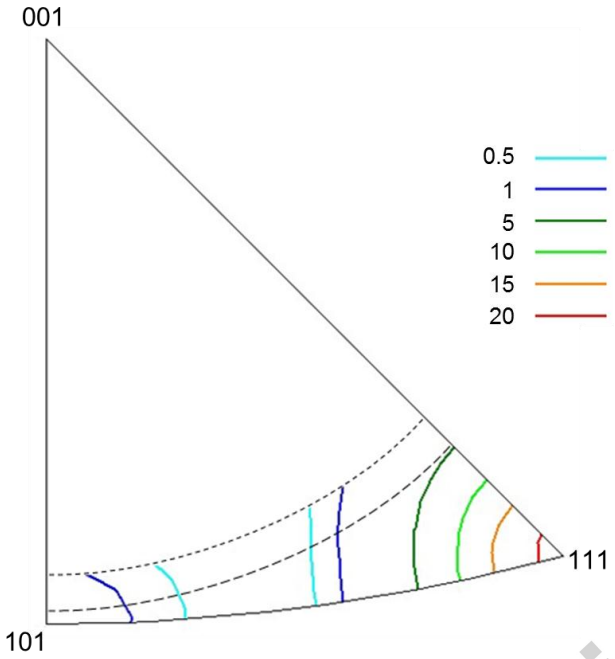

Fig. 11. Contour plot of the MDF from the joint in Fig. 8. (c), for misorientation angles in the range of 58-60º. The value of each contour line is expressed in multiples of uniform density. Also, the short and long dashed lines delimit the fundamental zone for 58 and 60º, respectively.

4.2.2. Epitaxial growth of the transient liquid phase

As it was shown in Fig. 8, both the joint and one of its neighbouring ferrite grains share the same parent austenite grain. This evidences the epitaxial growth during the TLPB process. However, the theoretical case in which both solidification fronts meet at the mid-thickness of the transient liquid phase at the end of the isothermal solidification stage in not taking place. In that case, the joint should be composed of at least two different parent austenite grains. Consequently, other approaches should be considered, namely:

- Temperature gradient-TLPB (TG-TLPB) [47]: by means of imposing a temperature gradient across the joint in lieu of a constant one, a directionally solidified TLPB can be achieved. It is well known that temperature gradients take place through induction heating [48]. However, heat input must be carried out under specific conditions to obtain the desired temperature gradient (e.g.:

along LD) [49]. Consequently, it is very unlikely that TG-TLPB has happened in this work.

- Grain growth during the holding time t at T_P: since TLPB process was carried out at 1300ºC, prior austenite grain (PAG) growth took place at the joint. This is evident in the FWHM of $\{100\}_\alpha$ from coarse ferrite grains of the base metal measured by XRTD (Fig. 6 (a)), which were formed from even coarser PAGs. PAGs growth during TLPB is described as follows (Fig. 12). Once the transient liquid phase has completed its solidification, PAGs are able to grow inside the joint without any restriction. At that point, some PAGs will grow at the expense of others, allowing portions of the joint to belong to a single parent austenite grain, as it was detected by EBSD (Fig. 8 (c) & (d)).

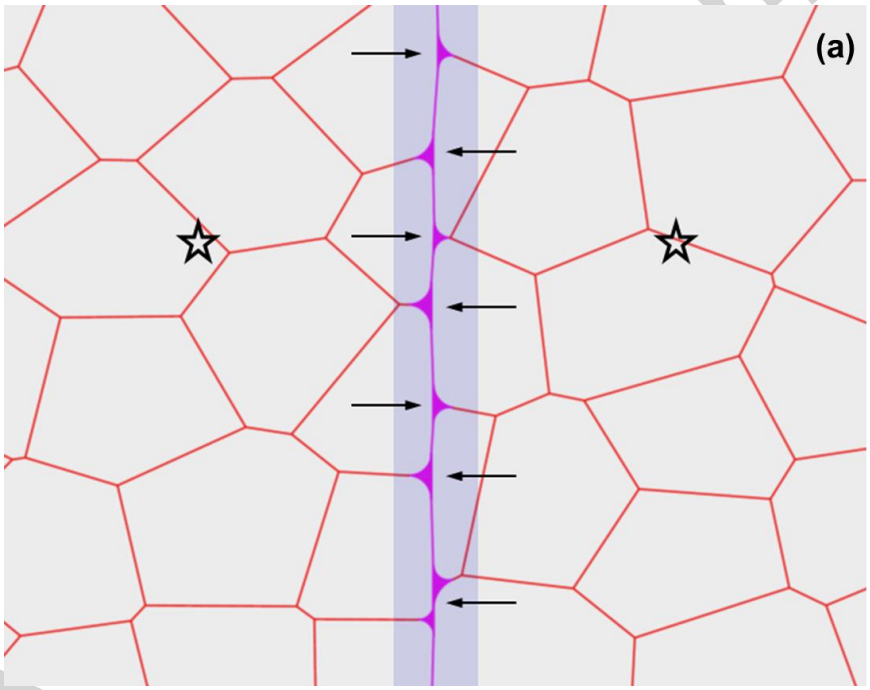

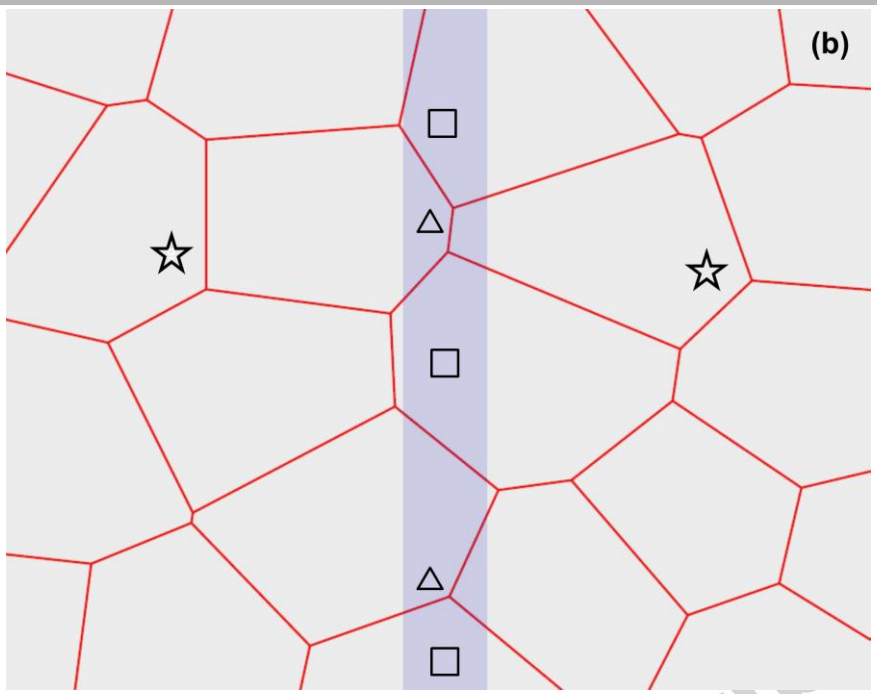

Fig. 12. Austenite grain growth during the holding time *t* at T_P. (a) Late stage of the isothermal solidification. Most of the transient liquid phase (violet coloured) at the joint (light-blue coloured) is penetrating PAG boundaries (arrow marks). PAGs from each of the pieces to be joined (star marks) are separated by the transient liquid phase. (b) PAGs' grain growth at the joint, after completion of isothermal solidification. Portions of the joint can belong to one PAG (square marks), or more PAGs (triangle marks).

4.2.3. Cellular structure of ferrite grains adjacent to the joint

Fig. 8 & 9 show coarse ferrite grains at each side of the joint, with a strong orientation spread. In addition, these grains resemble aggregations of subgrains, with a cell-block-like structure.

This type of structure was already reported when studying recrystallization of coarse-grained ferritic steels under a wide range of experimental conditions. For example, *Oudin et al* [50] reported this type of structure in Ti-stabilized interstitial free steel under warm deformation using hot torsion - in the ferritic range. Also, *Raabe et al* [51] obtained similar results in cold-rolled Nb-containing ferritic stainless steel. However, in this work cell blocks were identified - for the first time - in a ferritic steel through a tensile test carried out at room temperature.

The observed cellular structure of ferrite grains next to the joint confirms the presence of a significant plastic deformation developed during the tensile tests [10]. However, the deviation angle from the predicted near KS OR of bainite laths at the joint is within the reported range from undeformed samples. Thus, a distinguishable evidence of plastic deformation at the joint was not found due to the tensile test.

Despite this fact, decohesion of the joint/base metal interface is not detected, highlighting the strength and ductility of the bond.

5. Conclusions

TLPB of carbon steel bars, using Ni-based amorphous metallic foils as filler material, was performed. For the first time, its mechanical properties and microstructure were simultaneously characterized. The major results - for the selected base metal/filler material combination to replace TCs in SETs - are summarized as follows:

- The strength of the joint is above that of the HAZ, being the latter of at least 98.5 % of the UTS of the base metal. In addition, the attained ductility is in accordance with what is typically specified for steel arc-welded joints.
- A coalesced lath-like microstructure is observed at the joint, contrasting from that of the base metal. However, decohesion of the joint/base metal interface is not observed.
- Austenite transformation temperature ranges of all the observed microconstituents were measured by in situ XRTD. In particular, to determine the presence of coalesced bainite in lieu of martensite at the joint.
- Due to the chemical composition gradient across the joint, an abrupt microstructure change is observed. Thus, it renders impossible to determine only from visual inspection microconstituents from both the joint and the base metal that share the same parent austenite grain. However, and for the first time, OI analysis enabled to find definite

[10] Orientation spread can take place in coarse grains, plastically deformed or not.

experimental proof of the epitaxial nature of the TLPB process. In particular, that portions of the joint and its adjacent base metal can belong to a single parent austenite grain due to PAGs growth. This is in contrast to the theoretical case, in which the joint must be composed of at least two different parent austenite grains.

- For the first time, and by means of OI, cell block structures were identified in ferritic steel samples subjected to tensile test carried out at room temperature.

Acknowledgments

This work was supported by the Universidad de Buenos Aires [grant number. 20020130100515BA]. The authors acknowledge the XTMS beamline members, the LNLS, and the Brazilian Nanotechnology National Laboratory (LNNano) for the support with the diffraction experiments, and Metglas® for the donation of the filler material. The authors also wish to thank to Dr. Alberto Baruj (CNEA - CONICET), Dr. Gustavo Castellano (FaMAF, UNC - CONICET) and Dra. Silvina Limandri (FaMAF, UNC - CONICET).

Appendix

The 12 crystallographic variants for the NW orientation relationship [34].

Variant	Plane Parallel	Direction Parallel
V1	$(111)_\gamma$ // $(011)_\alpha$	$[2\bar{1}\bar{1}]_\gamma$ // $[0\bar{1}1]_\alpha$
V2		$[\bar{1}2\bar{1}]_\gamma$ // $[0\bar{1}1]_\alpha$
V3		$[\bar{1}\bar{1}2]_\gamma$ // $[0\bar{1}1]_\alpha$
V4	$(\bar{1}11)_\gamma$ // $(011)_\alpha$	$[\bar{2}\bar{1}\bar{1}]_\gamma$ // $[0\bar{1}1]_\alpha$
V5		$[12\bar{1}]_\gamma$ // $[0\bar{1}1]_\alpha$
V6		$[1\bar{1}2]_\gamma$ // $[0\bar{1}1]_\alpha$
V7	$(1\bar{1}1)_\gamma$ // $(011)_\alpha$	$[21\bar{1}]_\gamma$ // $[0\bar{1}1]_\alpha$
V8		$[\bar{1}\bar{2}\bar{1}]_\gamma$ // $[0\bar{1}1]_\alpha$
V9		$[\bar{1}12]_\gamma$ // $[0\bar{1}1]_\alpha$
V10	$(\bar{1}\bar{1}1)_\gamma$ // $(011)_\alpha$	$[2\bar{1}1]_\gamma$ // $[0\bar{1}1]_\alpha$
V11		$[\bar{1}21]_\gamma$ // $[0\bar{1}1]_\alpha$
V12		$[\bar{1}\bar{1}2]_\gamma$ // $[0\bar{1}1]_\alpha$

The 24 crystallographic variants for the KS orientation relationship [33].

Variant	Plane Parallel	Direction Parallel
V1	$(111)_\gamma$ // $(011)_\alpha$	$[\bar{1}01]_\gamma$ // $[\bar{1}\bar{1}1]_\alpha$
V2		$[\bar{1}01]_\gamma$ // $[\bar{1}1\bar{1}]_\alpha$
V3		$[01\bar{1}]_\gamma$ // $[\bar{1}\bar{1}1]_\alpha$
V4		$[01\bar{1}]_\gamma$ // $[\bar{1}1\bar{1}]_\alpha$
V5		$[1\bar{1}0]_\gamma$ // $[\bar{1}\bar{1}1]_\alpha$
V6		$[1\bar{1}0]_\gamma$ // $[\bar{1}1\bar{1}]_\alpha$
V7	$(1\bar{1}1)_\gamma$ // $(011)_\alpha$	$[10\bar{1}]_\gamma$ // $[\bar{1}\bar{1}1]_\alpha$
V8		$[10\bar{1}]_\gamma$ // $[\bar{1}1\bar{1}]_\alpha$
V9		$[\bar{1}0\bar{1}]_\gamma$ // $[\bar{1}\bar{1}1]_\alpha$
V10		$[\bar{1}0\bar{1}]_\gamma$ // $[\bar{1}1\bar{1}]_\alpha$
V11		$[011]_\gamma$ // $[\bar{1}\bar{1}1]_\alpha$
V12		$[011]_\gamma$ // $[\bar{1}1\bar{1}]_\alpha$
V13	$(\bar{1}11)_\gamma$ // $(011)_\alpha$	$[0\bar{1}1]_\gamma$ // $[\bar{1}\bar{1}1]_\alpha$
V14		$[0\bar{1}1]_\gamma$ // $[\bar{1}1\bar{1}]_\alpha$
V15		$[\bar{1}0\bar{1}]_\gamma$ // $[\bar{1}\bar{1}1]_\alpha$
V16		$[\bar{1}0\bar{1}]_\gamma$ // $[\bar{1}1\bar{1}]_\alpha$
V17		$[110]_\gamma$ // $[\bar{1}\bar{1}1]_\alpha$
V18		$[110]_\gamma$ // $[\bar{1}1\bar{1}]_\alpha$
V19	$(11\bar{1})_\gamma$ // $(011)_\alpha$	$[\bar{1}10]_\gamma$ // $[\bar{1}\bar{1}1]_\alpha$
V20		$[\bar{1}10]_\gamma$ // $[\bar{1}1\bar{1}]_\alpha$
V21		$[0\bar{1}\bar{1}]_\gamma$ // $[\bar{1}\bar{1}1]_\alpha$
V22		$[0\bar{1}\bar{1}]_\gamma$ // $[\bar{1}1\bar{1}]_\alpha$
V23		$[101]_\gamma$ // $[\bar{1}\bar{1}1]_\alpha$
V24		$[101]_\gamma$ // $[\bar{1}1\bar{1}]_\alpha$

Data availability

The raw data required to reproduce these findings are available to download from http://dx.doi.org/10.17632/yzzkvw82hc.1.

References

[1] M.K. Adam, M.A. Carmody, M.J. Jabs, R.S. O'Brien, D.G. Jiral, H.E. Payne, US Patent 8186427 B2 - One trip cemented expandable monobore liner system and method, (2012).

[2] R.M. Whiddon, US Patent 9163468 B2 - Expandable casing patch, (2015).

[3] O.S. Al-Abri, T. Pervez, M.H. Al-Maharbi, R. Khan, Microstructure evolution of

ultra-fine grain low-carbon steel tubular undergoing radial expansion process, Mater. Sci. Eng. A. 654 (2016) 94–106. doi:10.1016/j.msea.2015.12.016.

[4] F.C. Bennett, US Patent Application 2015/0285009 A1, (2015).

[5] R. LeBedz, R. Whiddon, US Patent Application 2010/0132956 A1, (2010).

[6] G.J. Hashem, US Patent 7621570 B2 - Pre-expanded connector for expandable downhole tubulars, (2009).

[7] D. S. Duvall, W. A. Owczarski, D. F. Paulonis, TLP Bonding: a New Method for Joining Heat Resistant Alloys, Weld. J. 53 (1974) 203–214.

[8] I. Tuah-Poku, M. Dollar, T.B. Massalski, A study of the transient liquid phase bonding process applied to a Ag/Cu/Ag sandwich joint, Metall. Trans. A. 19 (1988) 675–686. doi:10.1007/BF02649282.

[9] T. Shimizu, H. Horio, K. Kitou, S. Inagaki, R. Yamada, US Patent 6,378,760 - Method for manufacturing joint of carbon steel pipes suitable for expansion and expanding method, (2002).

[10] T. Shimizu, H. Horio, K. Kito, S. Inagaki, R. Yamada, US6592154 - Metal-pipe bonded body, pipe expansion method of metal-pipe bonded body, and method for inspecting metal-pipe bonded body, (2003).

[11] S.J. Chen, H.J. Tang, X.T. Jing, Transient liquid-phase bonding of T91 steel pipes using amorphous foil, Mater. Sci. Eng. A. 499 (2009) 114–117. doi:10.1016/j.msea.2007.11.133.

[12] X. Wang, X. Li, C. Wang, Effect of two-step heating process on joint microstructure and properties during transient liquid phase bonding of dissimilar materials, Mater. Sci. Eng. A. 560 (2013) 711–716. doi:10.1016/j.msea.2012.10.018.

[13] N. Di Luozzo, M. Fontana, B. Arcondo, Transient liquid phase bonding of steel using an Fe–B interlayer: microstructural analysis, J. Mater. Sci. 43 (2008) 4938–4944. doi:10.1007/s10853-008-2720-0.

[14] N. Di Luozzo, B. Doisneau, M. Boudard, M. Fontana, B. Arcondo,

Microstructural and mechanical characterizations of steel tubes joined by transient liquid phase bonding using an amorphous Fe–B–Si interlayer, J. Alloys Compd. 615 (2014) S18–S22. doi:10.1016/j.jallcom.2013.11.161.

[15] N. Di Luozzo, M. Boudard, B. Doisneau, M. Fontana, B. Arcondo, Transient liquid phase bonding of carbon steel tubes using a Cu interlayer: Characterization and comparison with amorphous Fe–B–Si interlayer bonds, J. Alloys Compd. 615 (2014) S13–S17. doi:10.1016/j.jallcom.2013.11.165.

[16] N. Di Luozzo, M. Boudard, M. Fontana, B. Arcondo, Effective diffusion coefficient for Cu in steel joined by transient liquid phase bonding, Mater. Des. 92 (2016) 760–766. doi:10.1016/j.matdes.2015.12.101.

[17] N.R. Philips, C.G. Levi, a. G. Evans, Mechanisms of Microstructure Evolution in an Austenitic Stainless Steel Bond Generated Using a Quaternary Braze Alloy, Metall. Mater. Trans. A. 39 (2007) 142–149. doi:10.1007/s11661-007-9382-4.

[18] J. Ruiz-Vargas, N. Siredey-Schwaller, N. Gey, P. Bocher, a. Hazotte, Microstructure development during isothermal brazing of Ni/BNi-2 couples, J. Mater. Process. Technol. 213 (2013) 20–29. doi:10.1016/j.jmatprotec.2012.07.016.

[19] W. Kurz, D.J. Fisher, Fundamentals of solidification, Trans Tech Publications, 1986.

[20] ASTM E8 / E8M - 13a, Standard Test Methods for Tension Testing of Metallic Materials, (2013). doi:10.1520/E0008_E0008M.

[21] BS EN ISO 7438:2016, Metallic materials. Bend test, (2016). doi:10.3403/30316722.

[22] BS EN ISO 5173:2010+A1:2011, Destructive tests on welds in metallic materials. Bend tests, (2010). doi:10.1017/CBO9781107415324.004.

[23] S.S. Babu, E.D. Specht, S.A. David, E. Karapetrova, P. Zschack, M. Peet, H.K.D.H. Bhadeshia, In-situ observations of lattice parameter fluctuations in austenite and transformation to bainite, Metall. Mater. Trans. A. 36 (2005) 3281–3289. doi:10.1007/s11661-005-0002-x.

[24] E. Keehan, L. Karlsson, O.H. Andrén, H.K.D.H. Bhadeshia, New Developments with C-Mn-Ni High-Strength Steel Weld Metals, Part A - Microstructure, Weld. J. 85 (2006) 200–210.

[25] H. Pous-Romero, H. Bhadeshia, Coalesced Martensite in Pressure Vessel Steels, J. Press. Vessel Technol. 136 (2014) 31402–31406. http://dx.doi.org/10.1115/1.4026192.

[26] E. V. Pereloma, I.B. Timokhina, S.P. Swenser, Formation of cementite in tempered Fe-Co-C alloys, Micron. 32 (2001) 825–829. doi:10.1016/S0968-4328(00)00090-1.

[27] A.W. Bowen, G.M. Leak, Solute diffusion in alpha- and gamma-iron, Metall. Trans. 1 (1970) 1695–1700. doi:10.1007/BF02642019.

[28] B.Y.C. Wells, Metals Technology, 1941, Vol. VIII - January 1941 - T.P. 1281 - Rate of Diffusion of Nickel in Gamma Iron in Low- carbon and High-carbon Nickel Steels, 281 (1941).

[29] G.F. Vander Voort, Atlas of Time-temperature Diagrams for Irons and Steels, ASM International, 1991.

[30] T.A. Palmer, J.W. Elmer, Direct observations of the $\alpha \rightarrow \gamma$ transformation at different input powers in the heat-affected zone of 1045 C-Mn steel Arc welds observed by spatially resolved X-ray diffraction, Metall. Mater. Trans. A Phys. Metall. Mater. Sci. 36 (2005) 3353–3369. doi:10.1007/s11661-005-0010-x.

[31] S. Babu, E. Specht, S.A. David, E. Karapetrova, P. Zschack, M. Peet, H. Bhadeshia, Time-resolved X-ray diffraction investigation of austenite and transformation to bainite, 1st Int. Symp. Steel Sci. (2007) 93–99. http://cml.postech.ac.kr/2008/I9-Babu.pdf.

[32] H.J. Stone, M.J. Peet, H.K.D.H. Bhadeshia, P.J. Withers, S.S. Babu, E.D. Specht, Synchrotron X-ray studies of austenite and bainitic ferrite, Proc. R. Soc. A Math. Phys. Eng. Sci. 464 (2008) 1009–1027. doi:10.1098/rspa.2007.0201.

[33] H. Kitahara, R. Ueji, N. Tsuji, Y. Minamino, Crystallographic features of lath martensite in low-carbon steel, Acta Mater. 54 (2006) 1279–1288.

doi:10.1016/j.actamat.2005.11.001.

[34] H. Kitahara, R. Ueji, M. Ueda, N. Tsuji, Y. Minamino, Crystallographic analysis of plate martensite in Fe-28.5 at.% Ni by FE-SEM/EBSD, Mater. Charact. 54 (2005) 378–386. doi:10.1016/j.matchar.2004.12.015.

[35] S. Morito, H. Tanaka, R. Konishi, T. Furuhara, T. Maki, The morphology and crystallography of lath martensite in Fe-C alloys, Acta Mater. 51 (2003) 1789–1799. doi:10.1016/S1359-6454(02)00577-3.

[36] J.-Y. Cho, D.-W. Suh, J.-H. Kang, H.-C. Lee, Orientation Distribution of Proeutectoid Ferrite Nucleated at Prior Austenite Grain Boundaries in Vanadium-added Steel, ISIJ Int. 42 (2002) 1321–1323. doi:10.2355/isijinternational.42.1321.

[37] C.P. Scott, J. Drillet, A study of the carbon distribution in retained austenite, Scr. Mater. 56 (2007) 489–492. doi:10.1016/j.scriptamat.2006.11.033.

[38] S.-J. Lee, Y.-K. Lee, Quantitative analyses of ferrite lattice parameter and solute Nb content in low carbon microalloyed steels, Scr. Mater. 52 (2005) 973–976. doi:10.1016/j.scriptamat.2005.01.028.

[39] S.M.C. Van Bohemen, The nonlinear lattice expansion of iron alloys in the range 100-1600 K, Scr. Mater. 69 (2013) 315–318. doi:10.1016/j.scriptamat.2013.05.009.

[40] K.A. Taylor, S.S. Hansen, The boron hardenability effect in thermomechanically processed, direct-quenched 0.2 Pct C steels, Metall. Trans. A. 21 (1990) 1697–1708. doi:10.1007/BF02672586.

[41] J. Ågren, Computer simulations of the austenite/ferrite diffusional transformations in low alloyed steels, Acta Metall. 30 (1982) 841–851. doi:10.1016/0001-6160(82)90082-7.

[42] H. Terasaki, Y.I. Komizo, Diffusional and displacive transformation behaviour in low carbon-low alloy steels studied by a hybrid in situ observation system, Scr. Mater. 64 (2011) 29–32. doi:10.1016/j.scriptamat.2010.08.055.

[43] J. Ågren, A thermodynamic analysis of the Fe-C and Fe-N phase diagrams,

Metall. Trans. A. 10 (1979) 1847–1852. doi:10.1007/BF02811728.

[44] Y.K. Lee, Empirical formula of isothermal bainite start temperature of steels, J. Mater. Sci. Lett. 21 (2002) 1253–1255. doi:10.1023/A:1016555119230.

[45] C. Capdevila, F.G. Caballero, C.G. de Andrés, Determination of martensite-start temperature in steels: Bayesian neural network model, ISIJ Int. 42 (2002) 894–902. doi:10.2355/isijinternational.42.894.

[46] A. Lambert-Perlade, A.F. Gourgues, A. Pineau, Austenite to bainite phase transformation in the heat-affected zone of a high strength low alloy steel, Acta Mater. 52 (2004) 2337–2348. doi:10.1016/j.actamat.2004.01.025.

[47] H. Assadi, Transient liquid phase diffusion bonding under a temperature gradient: modelling of the interface morphology, Acta Mater. 49 (2001) 31–39. doi:10.1016/S1359-6454(00)00307-4.

[48] N. Di Luozzo, M. Fontana, B. Arcondo, Modelling of induction heating of carbon steel tubes: Mathematical analysis, numerical simulation and validation, J. Alloys Compd. 536 (2012) S564–S568. doi:10.1016/j.jallcom.2011.12.084.

[49] A.A. Shirzadi, E.R. Wallach, US6257481 - Metal bonding, (2001).

[50] A. Oudin, P.D. Hodgson, M.R. Barnett, EBSD analysis of a Ti-IF steel subjected to hot torsion in the ferritic region, Mater. Sci. Eng. A. 486 (2008) 72–79. doi:10.1016/j.msea.2007.09.045.

[51] R.P. De Siqueira, H.R.Z. Sandim, D. Raabe, Particle stimulated nucleation in coarse-grained ferritic stainless steel, Metall. Mater. Trans. A Phys. Metall. Mater. Sci. 44 (2013) 469–478. doi:10.1007/s11661-012-1408-x.

[52] G. Nolze, R. Hielscher, Orientations - Perfectly colored, J. Appl. Crystallogr. 49 (2016) 1786–1802. doi:10.1107/S1600576716012942.

[53] X.F. Gu, T. Furuhara, W.Z. Zhang, PTCLab: Free and open-source software for calculating phase transformation crystallography, J. Appl. Crystallogr. 49 (2016) 1099–1106. doi:10.1107/S1600576716006075.

[54] W. Zhou, Z.L. Wang, Scanning Microscopy for Nanotechnology: Techniques and

Applications, Springer New York, 2007.

[55] U.F. Kocks, C.N. Tomé, H.R. Wenk, Texture and Anisotropy: Preferred Orientations in Polycrystals and Their Effect on Materials Properties, Cambridge University Press, 1998.